

## RESEARCH ARTICLE

10.1002/2016JC012538

## Key Points:

- Optimized ocean, sea ice, and ice shelf simulation of Amundsen and Bellingshausen Seas
- Significantly better match with observations than previous modeling studies, especially for winter water
- Local surface heat loss may not fully explain the 2012 Pine Island Glacier melt decrease

## Correspondence to:

Y. Nakayama,  
yoshihiro.nakayama@jpl.nasa.gov

## Citation:

Nakayama, Y., D. Menemenlis, M. Schodlok, and E. Rignot (2017), Amundsen and Bellingshausen Seas simulation with optimized ocean, sea ice, and thermodynamic ice shelf model parameters, *J. Geophys. Res. Oceans*, 122, 6180–6195, doi:10.1002/2016JC012538.

Received 8 NOV 2016

Accepted 20 APR 2017

Accepted article online 25 APR 2017

Published online 3 AUG 2017

## Amundsen and Bellingshausen Seas simulation with optimized ocean, sea ice, and thermodynamic ice shelf model parameters

Y. Nakayama<sup>1,2</sup> , D. Menemenlis<sup>1</sup> , M. Schodlok<sup>1,3</sup>, and E. Rignot<sup>1,2</sup> 
<sup>1</sup>Jet Propulsion Laboratory, California Institute of Technology, Pasadena, California, USA, <sup>2</sup>Department of Earth System Science, University of California Irvine, Irvine, California, USA, <sup>3</sup>JIFRESSE, Joint Institute for Regional Earth System Science and Engineering, University of California Los Angeles, Los Angeles, California, USA

**Abstract** Recent studies suggest that the thickness of Winter Water (WW), that is, water with potential temperature below  $\sim -1^\circ\text{C}$  located below Antarctic Surface Water and above Circumpolar Deep Water (CDW) is critical in determining the ice shelf melt rate, especially for the Pine Island Glacier (PIG). Existing model studies, however, misrepresent WW thickness and properties in the Amundsen Sea (AS). Here, we adjust a small number of model parameters in a regional Amundsen and Bellingshausen Seas configuration of the Massachusetts Institute of Technology general circulation model in order to reproduce properties and thickness of WW and CDW close to observations, with significant improvement for WW compared to previous studies. The cost, which is defined as weighted model-data difference squared, is reduced by 23%. Although a previous modeling study points out that the local surface heat loss upstream from Pine Island Polynya could be the reason for the observed 2012 PIG melt decline and WW thickening, they did not show WW freshening, which was observed at the same time. Model sensitivity experiments for surface heat loss, PIG melt rate, and precipitation fail to replicate WW freshening concurrent with PIG melt decline, implying that these processes cannot fully explain the observed PIG melt decrease.

## 1. Introduction

The ice shelves and glaciers of the West Antarctic Ice Sheet (WAIS) are melting and thinning rapidly in the Amundsen Sea (AS) and Bellingshausen Sea (BS) [e.g., Pritchard *et al.*, 2012; Shepherd *et al.*, 2012; Depoorter *et al.*, 2013; Rignot *et al.*, 2013; Paolo *et al.*, 2015], with consequences for global sea level rise and ocean circulation. First, approximately 10% of the observed sea level rise has been attributed to the thinning of WAIS between 2005 and 2010 [Shepherd *et al.*, 2012]. A collapse of WAIS has the potential to raise global sea level by 3.3 m [Bamber *et al.*, 2009]. Second, the melting of ice shelves in AS and BS will freshen the shelf water locally as well as downstream in the Ross Sea (RS) [Nakayama *et al.*, 2014a], which may lead to a change in the characteristics of Antarctic Bottom Water (AABW) formed in the RS and thus influence the global thermohaline circulation [Jacobs *et al.*, 2002; Rintoul, 2007].

High basal melting of the WAIS ice shelves in the AS and BS sectors is caused by warm Circumpolar Deep Water (CDW, about  $0.5\text{--}1.5^\circ\text{C}$  located below  $\sim 300\text{--}500$  m), which intrudes onto the continental shelf via submarine glacial troughs located at the continental shelf break (Figure 1) [e.g., Jacobs *et al.*, 1996; Walker *et al.*, 2007; Jacobs *et al.*, 2011; Nakayama *et al.*, 2013; Walker *et al.*, 2013; Dutrieux *et al.*, 2014]. When this warm water flows into an ice shelf cavity and reaches the grounding line, it melts the glacier and forms a buoyant plume of CDW and meltwater. Above CDW, cold ( $\sim -1.5^\circ\text{C}$ ) and fresh (salinity  $< 34.4$ ) Winter Water (WW) [Dutrieux *et al.*, 2014] can be observed, which is seasonally replenished by interaction with atmosphere and sea ice.

Recently observations as well as modeling studies reveal that the depth of thermocline and the presence of a subglacial ridge (which rises up to 300 m above the surrounding bathymetry) beneath the Pine Island Glacier (PIG) are extremely important for controlling the PIG melt rate [Dutrieux *et al.*, 2014; De Rydt *et al.*, 2014]. Dutrieux *et al.* [2014] show that the amount of CDW reaching the PIG front was significantly reduced in 2012 due to the deepened thermocline. The thermocline depth is  $\sim 200$  m deeper in 2012 compared to other years (e.g., 1994, 2007, 2009, and 2010) [see Dutrieux *et al.*, 2014, Figure 2a], leading to a 50% PIG melt decrease in 2012. Since the thermocline is located at the interface between WW and CDW, the depression

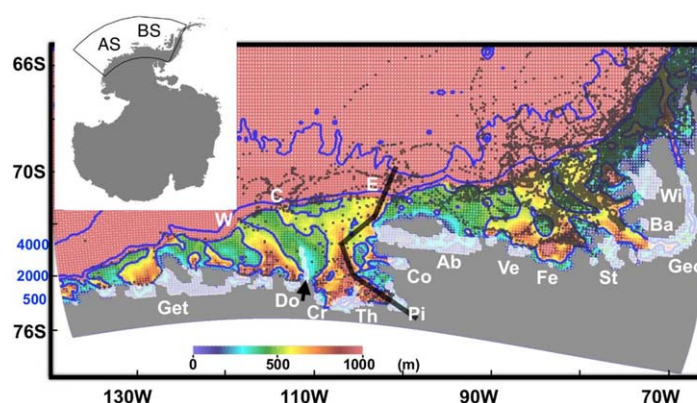


**Figure 1.** Horizontal grid of the model domain with the depth of the model bathymetry (color). Bathymetric contours of 500, 2000, and 4000 m are shown with blue contours. The inset (left top) shows Antarctica with the region surrounded by black line denoting the location of the enlarged portion. AS and BS denote the Amundsen and Bellingshausen Seas. White region with black arrow (between Do and Cr) indicates the location of grounded icebergs and landfast ice. This white region is treated as a barrier in the sea ice model and we do not allow sea ice exchange crossing this region. Black dots are the location of ship-based and seal CTD stations, which are used to compare model results with observations. Letters E, C, and W denote the submarine glacial troughs located on the eastern AS continental shelf. Location of ice shelves are shown with white patches and acronyms are summarized in Table 3. The thick black line represents the vertical section shown in Figures 2, 3, and 12.

remains similar to other years. *St-Laurent et al.* [2015] used numerical modeling to suggest that the increased surface heat loss in upstream areas of low ice concentration (polynyas) forms cold WW, which intrudes into the PIG cavity and contributes to the deepening of the thermocline and the PIG melt decrease in 2012. They, however, did not explain WW freshening observed at the same time. Recently, *Webber et al.* [2017] analyze the data from the mooring observations at the PIG front and show that a drop in

of the thermocline requires a mechanism that thickens WW between 2010 and 2012. The thickening of WW is associated with freshening of WW (deepening of the isohaline contour e.g., 34.2–34.5), as shown in Figures 2a and 2b in *Dutrieux et al.* [2014], who suggest that this WW thickening is caused by changes in local surface buoyancy and wind forcing through diapycnal exchanges and/or remote modifications in the atmosphere-ocean system. We note that this freshening, however, does not occur simply throughout the entire water column but is focused between 250 and 600 m [*Dutrieux et al.*, 2014, Figure 2a] and salinity at the shallower (<~250 m) or deeper (>~600 m) depths

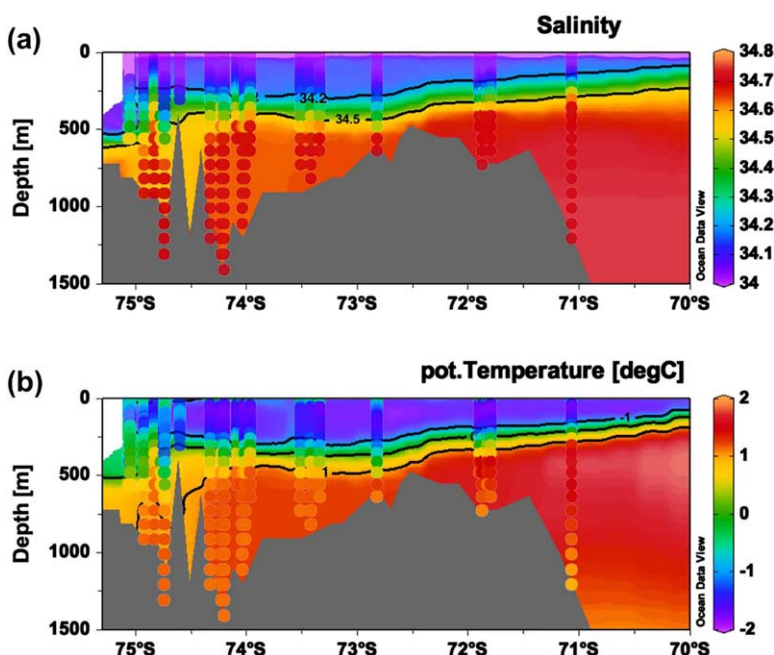


**Figure 2.** Simulated vertical sections of monthly mean (a) salinity and (b) potential temperature in January 2010 along the thick black line in Figure 1 for the optimized simulation. All the CTD profiles in 2010 within 50 km from the vertical section are plotted as circles with color indicating (a) salinity and (b) potential temperature of CTD observations. CTD data in other years show a similar pattern (see Figure 4 for horizontal distribution). For salinity, contours of 34.2 and 34.5 are shown with black lines. For potential temperature, contours of  $-1$ ,  $0$ , and  $1^\circ\text{C}$  are shown with black lines.

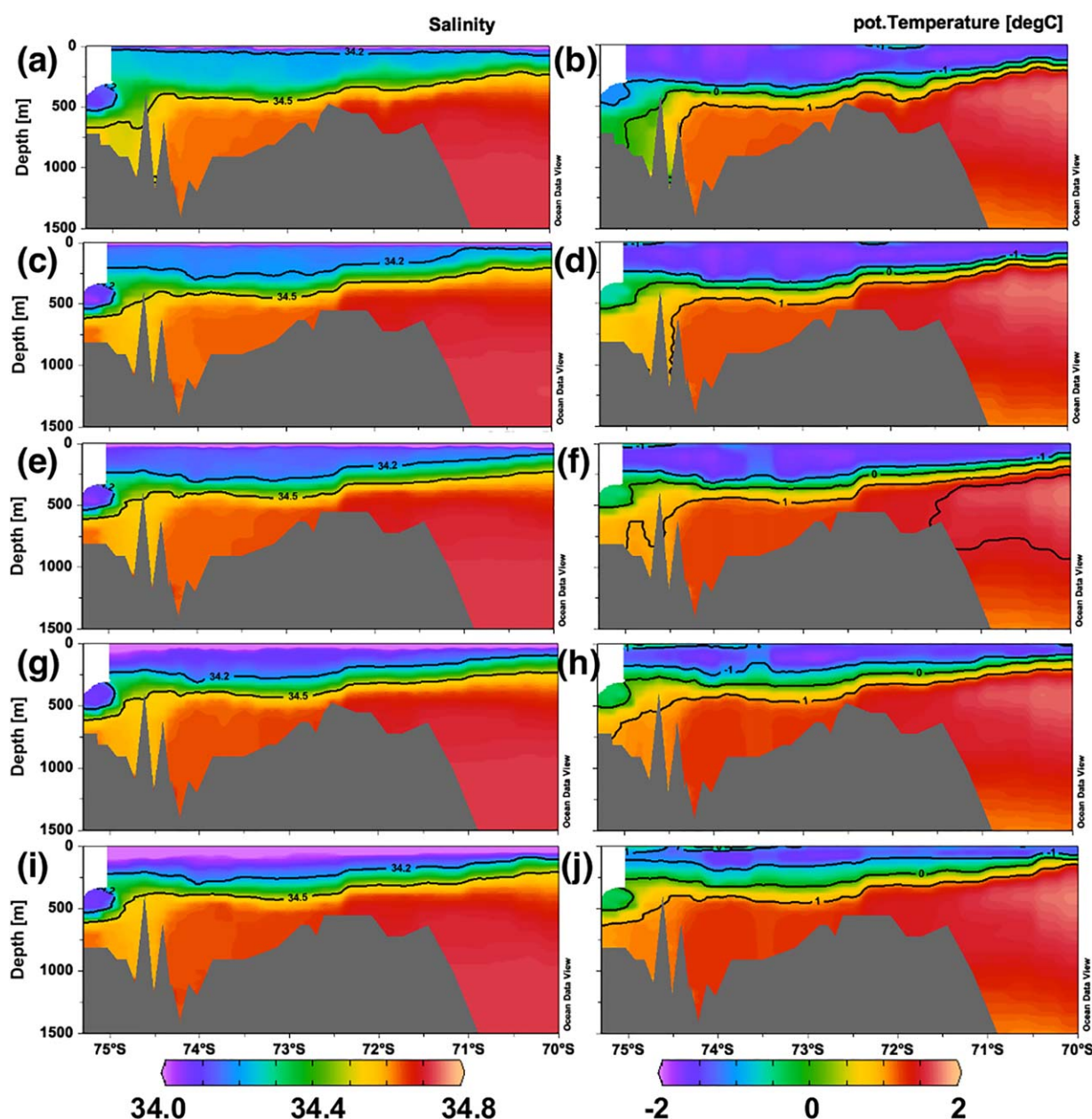


**Figure 3.** Simulated vertical sections of monthly mean (left) salinity in January 2010 along the thick black line in Figure 1 for the (a) SF120, (c) SF110, (e) optimized, (g) SF80, and (i) SF60 simulations and the same for monthly mean (right) potential temperature for the (b) SF120, (d) SF110, (f) Optimized, (h) SF80, and (j) SF60 simulations. For salinity, contours of 34.2 and 34.5 are shown (black lines). For potential temperature, contours of  $-1$ ,  $0$ , and  $1^{\circ}\text{C}$  are shown (black lines). For only (f) optimized simulation, a contour of  $1.5^{\circ}\text{C}$  is additionally shown for the location of Upper Circumpolar Deep Water (UCDW) for tracer experiments (Figure 9).

temperature corresponds to a decrease in salinity, which may be related to changes in surface heat flux and local ocean circulation.

Even though the importance of the thermocline is emphasized from several observational studies, none of the numerical simulations have shown a good representation of WW properties and thickness. In fact, most of the previous modeling studies evaluate their results based only on simulated CDW properties and intrusion pathways [e.g., Thoma *et al.*, 2008; Holland *et al.*, 2010; Schodlok *et al.*, 2012; Assmann *et al.*, 2013; Nakayama *et al.*, 2014a, 2014b; St-Laurent *et al.*, 2015; Rodriguez *et al.*, 2016] and there seem to exist difficulties in simulating realistic WW properties as well as thickness of WW. Previous modeling studies have not paid sufficient attention to WW thickness and salinity; some models seem to produce WW thicker than observed [e.g., Assmann *et al.*, 2013; Nakayama *et al.*, 2014b] while other models seem to produce too thin



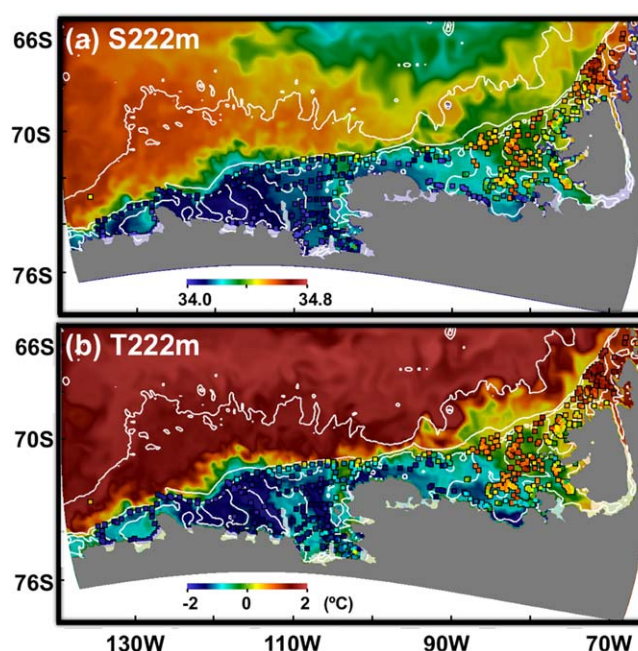


**Figure 4.** Simulated monthly mean (a) salinity and (b) potential temperature at 222 m depth in January 2010. Squares indicate the location of CTD and seal CTD data of 2007, 2009, and 2010, and the color of the squares shows their (a) salinity and (b) potential temperature at 222 m depth. Because of limited space in the figure, only 15% of the seal CTD profiles are plotted.

and properties) for the period of 2007–2010. We focus on this time period because summer observations in 2007, 2009, and 2010 show small interannual variability in the Eastern AS, including the PIG front (Figures 4 and 5), as pointed out by Nakayama *et al.* [2013]. Another objective of this study is to pave the way for coupled ocean-ice shelf optimization in the Estimating the Circulation and Climate of the Ocean (ECCO) project. We

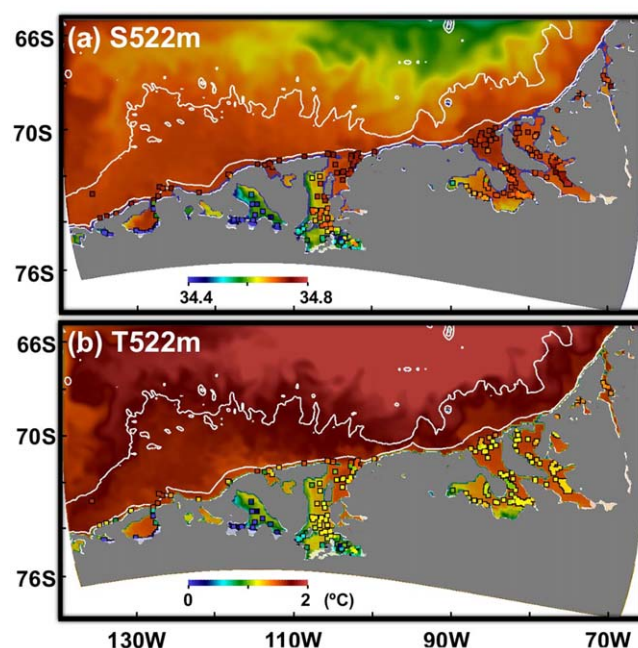


**Figure 5.** Same figures as in Figure 4 but for 552 m depth. Note that color ranges for potential temperature and salinity are different from Figure 4.

and too saline WW [e.g., Holland *et al.*, 2010; Schodlok *et al.*, 2012; St-Laurent *et al.*, 2015; Rodriguez *et al.*, 2016]. The recent regional modeling study of St-Laurent *et al.* [2015], for example, best simulates the properties as well as thickness of CDW but their WW is too saline (similar to Figures 3a and 3b). In their study, the 34.2 isohaline is located at depths between 100 and 200 m [see St-Laurent *et al.*, 2015, Figures 2a and 2b] while, based on the Conductivity-Temperature-Depth (CTD) observations of Dutrieux *et al.* [2014], the observed 34.2 isohaline is located near the ~250 m depth in 2010 (Figure 2a) and ~300 m depth in 2012. Since density of sea water is largely controlled by salinity at low temperature, correct representations of WW properties and its thickness are essential for investigating the processes controlling the depth of the thermocline and thus the PIG melt rate.

In this study, we aim to reproduce realistic WW and CDW (including thickness

and properties) for the period of 2007–2010. We focus on this time period because summer observations in 2007, 2009, and 2010 show small interannual variability in the Eastern AS, including the PIG front (Figures 4 and 5), as pointed out by Nakayama *et al.* [2013]. Another objective of this study is to pave the way for coupled ocean-ice shelf optimization in the Estimating the Circulation and Climate of the Ocean (ECCO) project. We therefore carry out our study in a subregion of the global Latitude-Longitude-polar Cap (LLC) 270 configuration [Forget *et al.*, 2015] that has been adopted for next-generation ECCO state estimates. Although the LLC270 horizontal and vertical resolutions are insufficient to resolve critical ocean-ice shelf interaction processes, e.g., eddy transport and mean flow topography interaction, this study is a first step toward improved parameterization and adjustment of these processes in the global ECCO LLC270 optimization.

After optimization, the simulation is able to realistically represent WW and CDW as well as the depth of the thermocline. The optimization was carried out by adjusting a small number of model parameters based on many forward sensitivity experiments and on a Green's functions approach [Ménemenlis *et al.*, 2005] as discussed below.

**Table 1.** Description of All the Sensitivity Simulations

Case	
SF120	Sensible and latent air-sea heat transfer coefficients multiplied by 1.2
SF110	Sensible and latent air-sea heat transfer coefficients multiplied by 1.1
SF80	Sensible and latent air-sea heat transfer coefficients multiplied by 0.8
SF60	Sensible and latent air-sea heat transfer coefficients multiplied by 0.6
PIG150	Ice shelf-ocean turbulent heat and salt exchange coefficients multiplied by 1.5
PIG50	Ice shelf-ocean turbulent heat and salt exchange coefficients multiplied by 0.5
Prep150	Precipitation multiplied by 1.5
Prep50	Precipitation multiplied by 0.5

and thermodynamic ice shelf [Losch, 2008] capabilities. The model domain contains the AS and BS (Figure 1). The grid is extracted from a global LLC270 configuration of the MITgcm. LLC270 is the grid selected for the next-generation ECCO ocean state estimation and has nominal horizontal grid spacing of  $1/3^\circ$ , compared to  $1^\circ$  for the LLC90 grid used for the ECCO version 4 solution. South of  $70^\circ\text{S}$ , the LLC270 configuration uses a bipolar grid; in the AS and BS domain, horizontal grid spacing is approximately 10 km (Figure 1) [Forget et al., 2015 for details]. The vertical discretization of the ECCO LLC270 configuration comprises 50 levels

**Table 2.** Model Parameters Used for Initial (LLC270) and Optimized Simulations<sup>a</sup>

Parameter	Initial Values	Optimized Values
Horizontal diffusivity	0	0
Background horizontal viscosity	0	0
Leith biharm nondimensional viscosity factor	2.0	2.0
Modified Leith biharm nondimensional viscosity factor	2.0	2.0
Background vertical diffusivity ( $\text{m}^2 \text{s}^{-1}$ )	$5.44 \times 10^{-7}$	$5.456 \times 10^{-6}$
Background vertical viscosity ( $\text{m}^2 \text{s}^{-1}$ )	$1.0 \times 10^{-4}$	$1.0 \times 10^{-4}$
KPP critical bulk Richardson Number		0.3273
KPP local Richardson Number limit for shear instability		0.8358
Bottom drag coefficient	$2.1 \times 10^{-3}$	$2.1 \times 10^{-3}$
Ocean/air drag coefficient scaling factor	1.0	0.508
Air/sea ice drag coefficient	$2.0 \times 10^{-3}$	$0.467 \times 10^{-3}$
Sea ice/ocean drag coefficient	$5.5 \times 10^{-3}$	$5.69 \times 10^{-3}$
Sea ice salt concentration	4.0	8.0
Stanton number (stable)	0.0327	0.0492
Stanton number (unstable)	0.0180	0.02506
Dalton number	0.0346	0.0520
Lead closing (m)	0.5	1.24
Ice strength ( $\text{N m}^{-2}$ )	$2.75 \times 10^4$	$1.97 \times 10^4$
Sea ice dry albedo	0.75	0.75
Sea ice wet albedo	0.66	0.698
Snow dry albedo	0.84	0.84
Snow wet albedo	0.7	0.672

<sup>a</sup>Initial values for critical bulk Richardson number and local Richardson number limit for shear instability are kept blank, because K-Profile Parameterization (KPP) is not used in the LLC270 simulation. Model parameters come from prior adjusted simulation and adjustments for some parameters are zero or close to zero because cost function is not sensitive to these parameters.

Following optimization, we present the results of several sensitivity studies (Table 1) associated with surface forcing and PIG melt rate parameters that are thought to influence thermocline depth at the PIG front. With these sensitivity studies, we investigate whether local atmospheric forcing is solely responsible for the thickening and freshening of WW and the PIG melt decrease observed between 2010 and 2012.

## 2. Description and Adjustment of Optimized Simulation

We use the Massachusetts Institute of Technology general circulation model (MITgcm), which includes dynamic/thermodynamic sea-ice [Losch et al., 2010]

varying in thickness from 10 m near the surface, 70–90 m in the 500–1000 m depth range, and 450 m at the deepest level of 6000 m. An optimization of the LLC270 configuration, similar to that described in Forget et al. [2015] for LLC90, is ongoing but does not yet include an explicit representation of ocean-ice shelf interactions.

Model bathymetry is based on International Bathymetric Chart of the Southern Ocean (IBCSO) [Arndt et al., 2013] and model ice draft is based on Antarctic Bedrock Mapping (BEDMAP-2) [Fretwell et al., 2013]. In addition, as shown by Nakayama et al. [2014b], several icebergs are grounded off the Bear Peninsula along the 400 m isobath forming a barrier of grounded icebergs and landfast ice limiting sea-ice transport between the eastern and central AS. Thus, we treat the region in white (see black arrow in Figure 1) as a barrier in the sea ice model. The model domain includes the George VI, Wilkins, Bach, Stange, Ferrigno, Venable, Abbot, Cosgrove, Pine Island, Thwaites, Crosson, Dotson, and Getz ice shelves (Figure 1).

Initial conditions are derived from a 10 year (2001–2010) spin-up of the model, integrated from rest and from January World Ocean Atlas 2009 temperature [Locarnini et al., 2010] and salinity [Antonov et al., 2010] fields. The spin-up uses the optimized parameters listed in Table 2, except for lead closing and background vertical diffusivity, which are set to 0.5 m and  $10^{-6} \text{m}^2 \text{s}^{-1}$ , respectively. Lateral boundary conditions for

hydrography, currents, and sea ice are provided by the ongoing ECCO LLC270 optimization. Surface forcing for the 2001–2010 period is provided by ECCO-v4 [Forger *et al.*, 2015], which is based on ERA-Interim [Dee *et al.*, 2011] and has been adjusted using the ECCO adjoint model-based methodology [Wunsch and Heimbach, 2013]. The mean differences between ECCO-v4 and ERA-interim over the eastern Amundsen Sea for air temperature, precipitation, and wind stress are, respectively,  $\sim -0.3^\circ\text{C}$ ,  $\sim -1 \times 10^{-9} \text{ m s}^{-1}$ , and  $\sim 1.5 \times 10^{-4} \text{ N m}^{-2}$  (negative values indicate that ECCO-v4 is smaller than ERA-interim). There is no additional freshwater run off above and beyond the meltwater computed by the MITgcm ice shelf package, that is, all calving icebergs are assumed to be transported and melt outside the regional AS and BS domain. The seventh-order advection scheme with monotonicity-preserving limiter of Daru and Tenaud [2004] is used for temperature and salinity advection. Horizontal viscosity follows the Leith Plus scheme of Fox-Kemper and Menemenlis [2008]. We set background horizontal viscosity to zero and use Leith Plus parameters for baseline and optimized runs. Note, however, that the flux-limited Daru and Tenaud [2004] advection scheme provides some implicit diffusivity and that the hydrography in the AS and BS is not very sensitive to horizontal diffusivity and viscosity. Bottom drag is quadratic with drag coefficient set to  $2.1 \times 10^{-3}$ .

Initial model parameters of the baseline simulation are shown in Table 2. The baseline simulation resulted in WW that was too saline relative to observations (not shown, similar to Figures 3a and 3b), similar to previous studies [e.g., St-Laurent *et al.*, 2015; Rodriguez *et al.*, 2016]. In order to achieve a better representation of WW and CDW, many forward simulations were conducted with different sets of model parameters and we used a combination of trial-and-error adjustments and a Green's function approach [Menemenlis *et al.*, 2005] to optimize the simulation. Specifically, we minimized a weighted least squares model-data misfit cost function,

$$J = \sum_{t=1}^{t_f} [\mathbf{y}(t) - \mathbf{E}(t)\mathbf{x}(t)]^T \mathbf{R}^{-1} [\mathbf{y}(t) - \mathbf{E}(t)\mathbf{x}(t)] \quad (1)$$

where  $\mathbf{y}(t)$  is a vector of observational data at time  $t$ ,  $\mathbf{x}(t)$  is the model state vector,  $\mathbf{E}(t)$  is a matrix that maps the model state space to the observation space, and  $\mathbf{R}^{-1}$  is a weight matrix that controls the relative contribution of different data sets to the cost function. Data constraints  $\mathbf{y}(t)$  include ship-based and seal CTDs, satellite-based estimates of sea ice concentration [Cavalieri *et al.*, 2006], and time-mean ice shelf melt rates from Rignot *et al.* [2013]. We assume diagonal error covariance matrix  $\mathbf{R}$ , where the diagonal elements  $\sigma^2$  are set to be variance of model output as a function of depth, 0.01, and estimated error squared from Rignot *et al.* [2013], respectively, for ship-based and seal CTDs, sea ice concentration, and time-mean ice shelf melt rates.

Overall the cost function was reduced by 23%, 16% via trial-and-error adjustments aimed at reducing the nonlinearity of the optimization problem, and 7% fine tuning via the Green's function approach. The optimized set of model parameters is shown on the right column of Table 2 and second column of Table 3.

**Table 3.** Satellite-Based Estimates of Basal Melt Rate [Rignot *et al.*, 2013] and Model Mean Basal Melt Rates (2004–2010) for West Antarctic Ice Shelves<sup>a</sup>

Name	$\gamma_T (\times 10^{-4} \text{ m s}^{-1})$	Observation-Based Estimates [Rignot <i>et al.</i> , 2013] (Gt yr <sup>-1</sup> )	Optimized Simulation (Gt yr <sup>-1</sup> )
George VI (Geo)	0.109	<b>89.0 ± 17</b>	<b>95.4</b>
Wilkins (Wi)	0.113	<b>18.4 ± 17</b>	<b>20.1</b>
Bach (Ba)	0.571	<b>10.4 ± 1</b>	<b>10.6</b>
Stange (St)	0.354	<b>28.0 ± 6</b>	<b>28.1</b>
Ferrigno (Fe)	2.21	<b>5.1 ± 2</b>	<b>5.6</b>
Venable (Ve)	0.348	<b>19.4 ± 2</b>	<b>20.2</b>
Abbot (Ab)	0.266	<b>51.8 ± 19</b>	<b>41.9</b>
Cosgrove (Co)	0.0786	<b>8.5 ± 2</b>	<b>9.3</b>
Pine Island (PI)	1.25	<b>101.2 ± 8</b>	<b>103.7</b>
Thwaites (Th)	0.918	<b>97.5 ± 7</b>	<b>94.3</b>
Crosson (Cr)	15.2	<b>38.5 ± 4</b>	<b>27.5</b>
Dotson (Do)	3.27	<b>45.2 ± 4</b>	<b>36.7</b>
Getz (Get)	0.262	<b>144.9 ± 14</b>	<b>148.6</b>

<sup>a</sup>The values of heat transfer coefficient  $\gamma_T$  used for the optimized simulation are also shown and can be compared to the initial value of  $1.0 \times 10^{-4} \text{ m s}^{-1}$ . The values of basal melt rates are shown in bold.

For the ocean component, we made the following parameter adjustments relative to baseline simulations. First, we turn off the Gent and McWilliams [1990], Redi [1982], and Nguyen *et al.* [2009] schemes used in the LLC270 simulation. Second, the TKE vertical mixing scheme of Gaspar *et al.* [1990] used in the ECCO LLC270 simulation is replaced with the K-Profile Parameterization (KPP) of Large *et al.* [1994]. Third, we increase background vertical diffusivity and adjust the KPP bulk and local Richardson number parameters in order to simulate WW properties closer to observations.

The adjusted parameters for surface forcing and sea ice are listed on Table 2, rows 10–22. For ocean-air momentum exchange, we use the bulk formula of Large and Yeager [2004] but the drag coefficient  $C_D$  is scaled by 0.508,

as indicated in Table 2. Air-ice drag coefficient is set to  $\sim 0.5 \times 10^{-3}$ , which is approximately half the typically used value. For example, *Holland et al.* [2010] used air-ice drag coefficient of  $\sim 1.0 \times 10^{-3}$ , but note that this led to overestimated sea ice drift speed close to the continent as in *Holland et al.* [2010]. Sensible and latent heat transfer coefficients (Stanton and Dalton numbers) are set to  $\sim 1.5$  times higher for the optimized simulation relative to the values of *Large and Pond* [1982]. Sea ice salt concentration is also set to higher than typical values. These atypical values compensate for simulation errors due to unresolved scales and inaccuracies in the model parameterizations and boundary conditions. The remaining adjusted parameters listed on Table 2 all fall within the range of typically used values and have smaller impact on the hydrography of the AS and BS simulation.

For the static ice shelf component, the freezing/melting process in the subice-shelf cavity is parameterized by the three-equation thermodynamics of *Hellmer and Olbers* [1989]. Likely due to the coarse horizontal and vertical resolutions in our configuration ( $\sim 10$  km) [e.g., *Schodlok et al.*, 2016], uncertainties in model bathymetry and ice draft [*Schodlok et al.*, 2012], and lack of tidal forcing, the simulated area averaged melt rates are very different compared to the *Rignot et al.* [2013] observations when we use the exchange coefficients of *Hellmer and Olbers* [1989] and *Jenkins et al.* [2001]. For example, melt rates for some ice shelves (e.g., George VI, Stange, Abbot, Cosgrove, and Getz) are overestimated by a factor of 2–4, while melt rates for other ice shelves (Pine Island, Crosson, and Dotson) are underestimated by about half. *Schodlok et al.* [2016] show that the coarse vertical resolution used in this study may overestimate ice shelf basal melt rates and the representation of a fresh/cold layer at the ice shelf base and of warm/salty water near the bottom can be improved with more vertical levels. Unusually low basal melt rates for Crosson and Dotson ice shelves are possibly related to highly inaccurate bathymetry in the vicinity, as pointed out recently by *Millan et al.* [2017]. In this study, we adjust turbulent heat and salt exchange coefficients for individual ice shelves to constrain the mean melt rates to be close to the satellite-based estimates of *Rignot et al.* [2013] (see Table 3). We note that the ratio of these two coefficients is maintained. For simplification and considering, the fact that  $\sim 10$  km horizontal grid spacing is not sufficient to resolve flow in the cavity, we only use parameterization as a function of temperature difference but not of ocean current at the ice shelf base.

Adjustment of turbulent heat and salt exchange coefficients for individual ice shelves is a convenient way to force the ocean model (especially with coarse resolution) with realistic amounts of freshwater flux from ice shelves for the following reasons: (1) model simulation has bias in the water mass characteristics in the cavity caused by processes not implemented or resolved in the model simulation, e.g., ocean mixing and tidal forcing; (2) basal melting parameterization includes uncertainty, e.g., treatment of mixed layer at the ice-ocean interface, bottom drag coefficient, etc. [*Jenkins et al.*, 2010]; (3) sensitivity of basal melt rate to the not well known ice shelf cavity shape. Since the strength of basal melting determines the strength of cavity circulation, large adjustments of heat and salt transfer coefficients (e.g., for George VI or Getz Ice Shelves) influence the strength of CDW intrusion and the CDW properties intruding into the ice shelf cavities (not shown) as recently pointed out by *Jourdain et al.* [2017].

### 3. Evaluation of Optimized Simulation

In this section, we evaluate results from the 2001–2010 optimized simulation, described above, using model-data comparisons and by examining pathways of CDW intrusion and spreading of glacier meltwater.

#### 3.1. Model-Data Comparison

As pointed out by several studies, CDW intrusion into the PIG cavity occurs both from the eastern trough (trough E) and the central trough (trough C) [*Walker et al.*, 2007; *Thoma et al.*, 2008; *Jacobs et al.*, 2011; *Schodlok et al.*, 2012; *Nakayama et al.*, 2013; *Walker et al.*, 2013; *Dutrieux et al.*, 2014]. CTD measurements following the CDW intrusion from trough E into the PIG have been repeatedly conducted in 2009 [*Jacobs et al.*, 2011, Figure 2] and 2010 [*Nakayama et al.*, 2013, Figure 4] and dots in Figure 2) showing similar vertical profiles with CDW below 400–500 m and WW above 250–400 m. The vertical section of the optimized simulation (thick black line in Figure 1) represents WW and CDW with realistic thickness and properties (Figure 2). The 34.2 salinity contour is located at  $\sim 250$  m depth, which is consistent with observations and showing significant improvement compared to previous modeling studies [e.g., *Nakayama et al.*, 2014b; *St-Laurent et al.*, 2015]. Slight differences can still be found for WW properties close to the surface ( $\sim 50$ –250 m) with salinity being still too saline ( $\sim 0.1$ ). CDW on the continental shelf close to the shelf break shows



good agreement with observations (e.g., at 72°S) but the difference becomes larger closer to the PIG front ( $\sim 0.1$  for salinity and  $\sim 0.2^\circ\text{C}$  for potential temperature, Figure 2).

Simulated January mean salinity and potential temperature in 2010 at the 222 m depth also show close agreement with ship-based and seal CTD data between 2007 and 2010, indicating that horizontal distribution of WW properties agree well with observations in most of the AS and BS (Figure 4). In the AS, the model captures similar spatial patterns as the observations. In the BS, a larger difference is observed in the central part ( $\sim 80^\circ\text{W}$ ) with simulated salinity and temperature underestimated by  $\sim 0.2$  and  $\sim 1^\circ\text{C}$ , respectively. This seems to be caused by the mismatch of the thermocline depth in the model. However, this model is still capable of capturing the increasing trend of temperature and salinity from the western to eastern parts of BS.

Simulated January mean salinity and potential temperature in 2010 at the 552 m depth in the AS show close agreement with ship-based and seal CTD data close to the shelf break (Figure 5), while CDW intrusion in the BS is warmer than observations possibly caused by the mismatch of the thermocline depth in the area. Differences for both salinity and potential temperature become large further onshore close to the continents both in the AS and BS, which is likely caused by the lack of horizontal resolution. Eddy transports [e.g., Schodlok et al., 2012; St-Laurent et al., 2013; Nakayama et al., 2014c; Stewart and Thompson, 2015] are considered to be important in transporting CDW onshore on the continental shelf and this can only be resolved with horizontal grid spacing of  $\sim 1\text{--}2$  km.

The optimized simulation shows similar interannual and seasonal variability as do the observations. Horizontal sections of salinity and potential temperature at the 222 m depth in January 2009 and 2010 (Figures 6 and 7) show fairly small difference, which is consistent with observations (small interannual variability) [Nakayama et al., 2013; Dutrieux et al., 2014]. Seasonal variability of the model is also consistent with previous model studies [e.g., St-Laurent et al., 2015, Figure 4a] with warmer ( $\sim 0.5^\circ\text{C}$ ) and more saline ( $\sim 0.05$ ) properties found at 222 m at the entrance of trough E in January than in July. Potential temperature and salinity at 552 m do not show large seasonal variability of CDW intrusion (not shown).

For sea ice in the optimized simulation, the modeled mean summer (March) sea ice extent is similar to satellite-based estimates [Cavalieri et al., 2006], while modeled mean winter (September) sea ice extent is overestimated by 16%. Similar to Schodlok et al. [2016], maximum sea ice extent is overestimated and retreat of sea ice is slower than satellite-based estimates (not shown).

Simulated monthly mean basal melt rates are nearly stable throughout the simulation period (Figure 8). Since we adjust the heat and salt transfer coefficients for ice shelves, the mean simulated basal melt rates match the values of Rignot et al. [2013] within error bars. For example, mean melt rates for George VI, Pine Island, Thwaites, and Getz Ice Shelves are 95.4, 103.7, 94.3, and 148.6  $\text{Gt yr}^{-1}$ , respectively (Table 3), consistent with other observation-based estimates [e.g., Jenkins and Jacobs, 2008; Jacobs et al., 2013; Depoorter

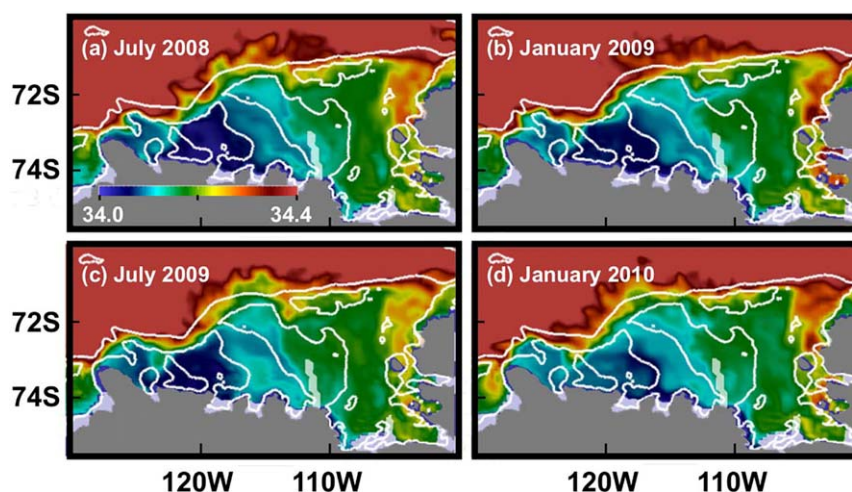


**Figure 6.** Simulated monthly mean salinity at 222 m depth for (a) July 2008, (b) January 2009, (c) July 2009, and (d) January 2010. Bathymetric contours of 500, 2000, and 4000 m are shown (white lines). Note that color range is different from Figure 4.



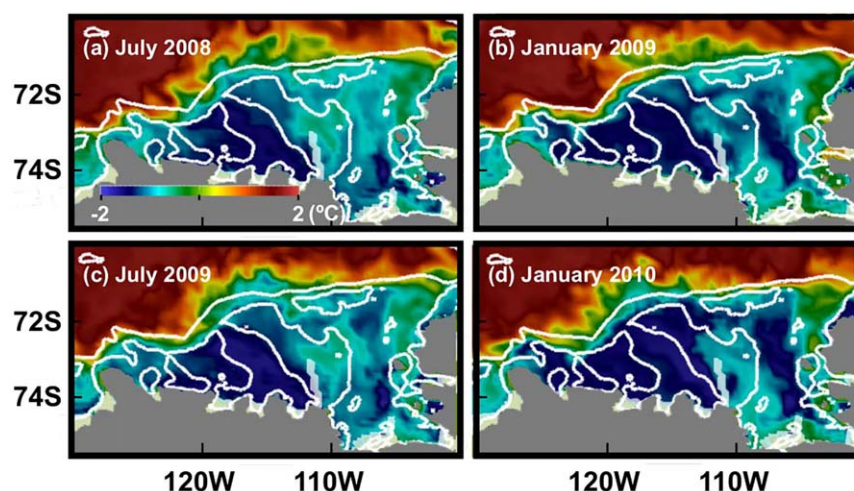


**Figure 7.** Simulated monthly mean potential temperature at 222 m depth for (a) July 2008, (b) January 2009, (c) July 2009, and (d) January 2010. Bathymetric contours of 500, 2000, and 4000 m are shown (white lines). Note that color range is different from Figure 4.

*et al.*, 2013; Nakayama *et al.*, 2013; Rignot *et al.*, 2013; Dutrieux *et al.*, 2014]. We point out that seasonal variability of melt rates is not large (e.g., 5–10 Gt yr<sup>−1</sup> for Pine Island Glacier), smaller than previous modeling studies (e.g., ~30 Gt yr<sup>−1</sup> for Schodlok *et al.* [2012] and St-Laurent *et al.* [2015]). This could be related to reduced seasonal variability of CDW intrusion due to insufficient horizontal resolution. Reduced air-ice drag coefficient and sea ice salt concentration in the optimized solution both lead to reduced brine rejection and vertical mixing in the coastal polynya, which may also be related to the reduced seasonal variability. However, the seasonal variability with higher melt in summer and lower melt in winter is consistent with St-Laurent *et al.* [2015].

Overall, despite the coarse horizontal resolution and the differences listed above, the representation of hydrography in the AS has significantly improved compared to previous modeling studies, especially for the properties and thickness of WW. Property and thickness of CDW is also well reproduced, but CDW intrusion on the continental shelf onshore is slightly weakened, most likely due to the lack of horizontal resolution. In the following subsection, we analyze pathways of CDW intrusion and spreading of glacier meltwater using passive tracers.

### 3.2. Pathway of CDW Intrusion

As described in previous studies, CDW can be divided into two types, Upper Circumpolar Deep Water (UCDW) and Lower Circumpolar Deep Water (LCDW). UCDW is characterized by subsurface nutrient maxima, low oxygen [Callahan, 1972; Sievers and Nowlin, 1984], and subsurface temperature maximum south of the polar front; while LCDW is characterized by salinity maxima [Smith *et al.*, 1999]. Based on T-S diagrams, UCDW and LCDW in the AS and BS can also be distinguished using potential temperature of 1.5°C [see

Smith *et al.*, 1999, Figure 2 and Nakayama *et al.*, 2013, Figure 6]. We use two virtual passive tracers, TR1 and TR2, to trace the intrusion of UCDW and LCDW, respectively, similar to Dinniman *et al.* [2011, 2012] for their study in the West Antarctic Peninsula. For TR1, initial tracer concentration is set to 1.0 for water off the continental shelf (the region deeper than 1200 m) at any depth with potential temperature higher than 1.5°C (1.5°C contour line is shown in Figure 3f). For TR2, the initial tracer concentration is set to 1.0 for water off the continental shelf at any

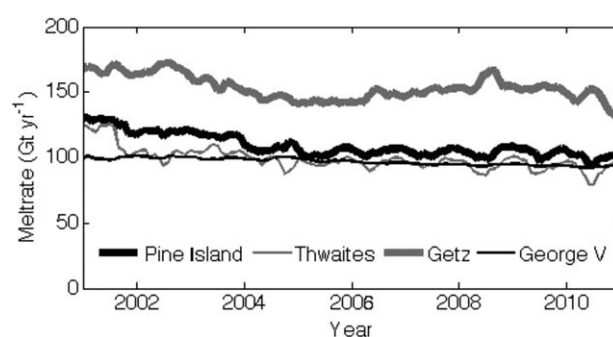


**Figure 8.** Simulated monthly mean basal ice melt rates from 2001 to 2010 for the Pine Island, Thwaites, Getz, and George VI Ice Shelves.

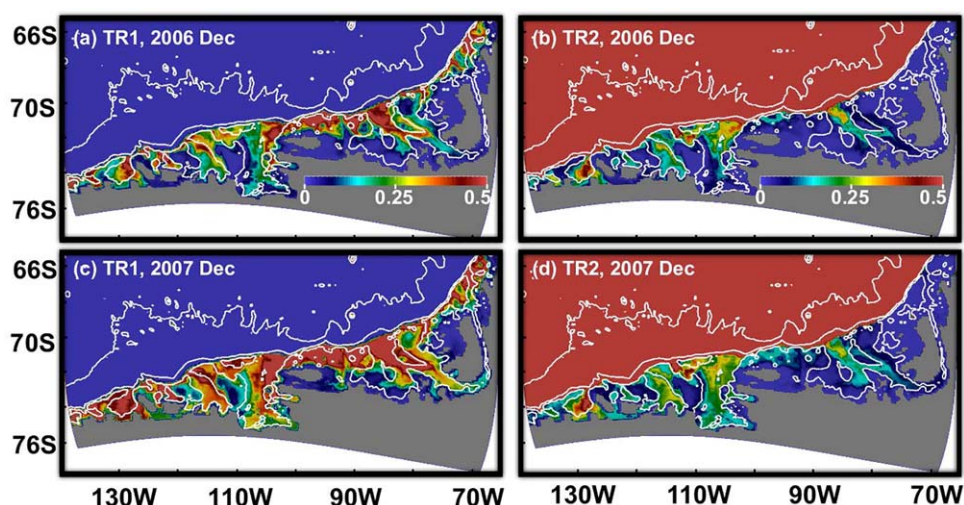


**Figure 9.** Bottom concentration of tracers representing (left) Upper Circumpolar Deep Water (TR1) and (right) Lower Circumpolar Deep Water (TR2) for December 2006 and December 2007.

depth below UCDW. The model simulation for these two tracers is conducted for 2 years, from January 2006 to December 2007.

Based on the bottom concentrations of TR1 and TR2, both UCDW and LCDW intrude onto the continental shelf through submarine glacial troughs in the AS and BS (Figure 9). Generally, intrusion of UCDW occurs much quicker than LCDW. After 2 years of simulation, TR1 concentrations at the ice shelf front of AS ice shelves are about 20–40%, while TR2 concentrations at the ice shelf front of AS ice shelves are mostly 10–

25%. For the eastern AS, CDW intrusion occurs mostly from troughs E and C (Figure 1), which is consistent with previous studies [Nakayama *et al.*, 2013; Dutrieux *et al.*, 2014]. Based on observations, Nakayama *et al.* [2013] show that CDW intrusion from trough C contains more LCDW than intrusion from trough E [Nakayama *et al.*, 2013, Figure 8], which is clearly represented in Figure 9. Since 222 m and 552 m potential temperature and salinity show good agreement in the eastern AS, CDW intrusion is likely well reproduced in the eastern AS.

### 3.3. Pathway of Spreading of Glacier Melt Water

Similar to Nakayama *et al.* [2014a], we use two virtual passive tracers to trace glacial meltwater from the AS and BS, which are released at the same rate as melting occurs at the ice shelf bases for 10 years from 2001 (Figure 10). Meltwater from the BS flows both eastward and westward, while glacial meltwater from the AS flows mainly westward towards the RS. After 10 years of simulation, about 62% of total

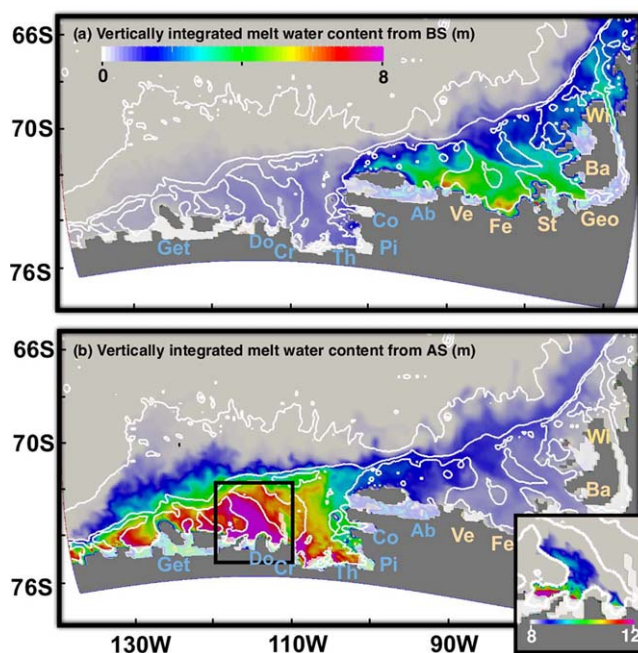


**Figure 10.** Spatial distributions of vertically integrated meltwater content after 10 years of optimized simulation showing the basal meltwater from (a) ice shelves in the BS (names in light yellow) and (b) ice shelves in the AS (names in light blue). The bathymetry contours of 500, 2000, and 4000 m are shown (white contours). Location of ice shelves are shown with white patches and acronyms are summarized in Table 3. The inset (right bottom) shows a close-up of meltwater (note the different color scale) for the central AS region.

glacial meltwater released from the ice shelves in the BS stays in the BS and 6% of glacial meltwater from BS reaches the AS. About 30% of BS glacial meltwater flows out of the model domain from the eastern and northern boundaries along the path of the Antarctic Circumpolar Current. Total glacial meltwater released from the ice shelves in the AS mostly flows westward with 38% remaining in the AS (east of 134°W and west of 100°W) and more than 50% flows out of the model domain from the western boundary toward the RS. Only 7% flows eastward reaching the BS (east of 100°W). This result is similar to Nakayama *et al.* [2014a] and emphasizes the importance of ice shelves in the AS as a potential reason for the freshening observed in the RS [Jacobs *et al.*, 2002, 2013; Nakayama *et al.*, 2014a].

The spatial distribution of meltwater also agrees with observations. For the AS, Randall-Goodwin *et al.* [2015] show that the observed vertically integrated meltwater content in front of Getz Ice Shelf (116–114°W) is ~10–14 m. Our results show concentrated melt at the same location (bottom right inset in Figures 10b and 11 in Randall-Goodwin *et al.* [2015]) and the vertically integrated melt is reaching 10 m, approximately 100 km off the ice shelf front and ~12 m at the ice shelf front, consistent with observations. Nakayama *et al.* [2013] also estimated pathways of glacial meltwater using CTD observations between 2007 and 2010, showing spreading of glacial meltwater from PIG toward the west along the bathymetry [Nakayama *et al.*, 2013, Figure 8], which is well reproduced in the model (Figure 10b). Kim *et al.* [2016] also show high concentration of dissolved helium at the Dotson ice shelf front and a similar spatial pattern is also reproduced in our model simulation. For the BS, Zhang *et al.* [2016] shows thick melt water mixture close to the coast in the vicinity of Venable, Ferrigno, and Stange ice shelves, and our model results also represent similar features.

#### 4. Sensitivity Studies

In this section, we conduct sensitivity studies to investigate the impact of sensible and latent heat fluxes, PIG melt rate, and precipitation on the properties and thickness of WW in the Eastern AS (Table 1). In these sensitivity simulations, we aim to make clear if these components of the atmospheric forcing can replicate the freshening and thickening of WW, which were observed at the PIG front between 2010 and 2012 together with the PIG melt decrease. For all sensitivity simulations, all other model parameters are kept the same as in the optimized simulation. All the sensitivity simulations are initialized on 1 January 2006 from the optimized simulation and we conduct model simulations for 5 years. We note that hydrographic properties in the AS in January 2006 are similar to 2010 (not shown).

##### 4.1. Effect of Sensible and Latent Heat Flux

For the sensitivity study on surface sensible and latent heat fluxes, four simulations with different sensible and latent heat transfer coefficients (SF120, SF110, SF80, and SF60) are performed (Table 1). For the SF120, SF110, SF80, and SF60 sensitivity simulations, sensible and latent heat transfer coefficients (Table 2) are multiplied by 1.2, 1.1, 0.8, and 0.6, respectively. Several studies have shown that the atmospheric AS low is controlled by tropical forcing [e.g., Steig *et al.*, 2012; Li *et al.*, 2014] and its location as well as magnitude are likely to change in the future [Turner *et al.*, 2013; Hosking *et al.*, 2016]. Since sensible and latent heat fluxes are a function of air temperature, humidity, and wind speed near the air-ocean interface, such changes in sensible and latent heat fluxes are very likely.

When sensible and latent heat transfer coefficients are large (small) as in the SF120 and SF110 (SF80 and SF60) sensitivity simulations, WW properties become colder (warmer) and saltier (fresher) and the depth of the thermocline becomes deeper (shallower), based on the vertical sections along the thick black line in Figure 1 (see Figure 3). In addition, properties of WW depend rather nonlinearly on the sensible and latent heat transfer coefficients. For example, the depth of the 34.2 and 34.5 isohalines do not change much for the SF110, optimized, SF80, and SF60 simulations (Figures 3c, 3e, 3g, and 3i), while the depth of the 34.2 isohaline is located at a depth of less than 50 m in the SF120 simulation (Figures 3a and 3b). Summer (March) sea ice extent responds rather linearly to sensible and latent heat transfer coefficients. Sea ice extent increases by ~20,000 km<sup>2</sup> and ~10,000 km<sup>2</sup> for, respectively, SF120 and SF110 relative to the optimized simulation. Winter (September) sea ice extent remains similar for all cases (not shown). CDW intrusion becomes stronger with smaller surface heat fluxes (e.g., 1°C contours of all the sensitivity simulations in Figure 3). As pointed out by St-Laurent *et al.* [2015], our simulations also show deepening of thermocline and PIG melt rate decline with increasing surface heat flux. PIG melt rates are 21.0, 82.5, 101.7, 117.4, and 122.9



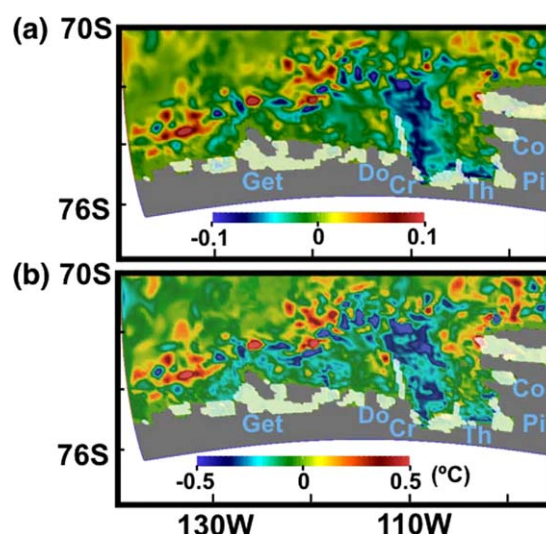


**Figure 11.** Simulated horizontal sections of the difference between the PIG150 and PIG50 sensitivity simulations (PIG150-PIG50) for monthly mean (a) salinity and (b) potential temperature in January 2010 at 299 m depth. Locations of ice shelves are shown with white patches and acronyms are summarized in Table 3.

Gt/yr for the SF120, SF110, SF80, and SF60 sensitivity simulations, respectively. However, even if the PIG melt decrease is replicated, we do not replicate the observed WW freshening.

#### 4.2. Effect of PIG Melting

Two sensitivity simulations with different PIG melt rates (PIG150 and PIG50) are performed (Table 1). For the PIG150 and PIG50 simulations, turbulent heat and turbulent salt exchange coefficients of PIG (see Table 3) are multiplied by 1.5 and 0.5, respectively. As a result, mean melt rates of PIG in 2010 are calculated to be 131.3 and 61.0 Gt yr<sup>-1</sup> for the PIG150 and PIG50 simulations, respectively.

Vertical sections of potential temperature and salinity differences between the PIG150 and PIG50 simulations show that the differences are small compared to other sensitivity studies, despite the large change in mean melt rates of PIG (not shown). This indicates that the short-term variability of basal melt rate does not have

a large impact on oceanic properties (such as depth of thermocline) along this section. The apparent lack of impact on the oceanic properties is because this particular section is located along the pathway of CDW intrusion but not the pathway of glacial melt water (Figures 9 and 10), and thus represents water that has not yet been in contact with the PIG.

Although the change in WW properties is not significant in Pine Island Bay, the influence of melting spreads downstream toward the RS. The potential temperature and salinity anomalies at the 299 m depth show freshening and cooling almost in the entire region of the Eastern AS (Figure 11). Freshening of 0.05 and cooling of 0.3°C can be observed downstream (~110°W) in the central part of AS. These results indicate that the magnitude of melting does not have a large impact on WW properties and thickness at the PIG front but it does thicken the WW layer to some extent (around 50 m or less) downstream. This also implies that freshening and cooling near PIG may be caused by an increase in basal melt rates of other glaciers upstream of PIG. Due to this spreading of glacial meltwater, melt rates for Thwaites, Crosson, Dotson, and Getz ice shelves are, respectively, 93.1 (89.3), 30.6 (22.6), 30.9 (25.6), and 153 (146) Gt yr<sup>-1</sup> for the PIG50 (PIG150) simulation. This indicates that an increase in melt rate in one ice shelf reduces melt rates of other ice shelves downstream (by ~5–20% when comparing the PIG150 and PIG50 simulations) but the influence on other ice shelves is not large.

#### 4.3. Effect of Precipitation

Two sensitivity simulations (Prep150 and Prep50) with increased (150%) and decreased (50%) precipitation are also conducted (Table 1). Considering that the adjustment made between ERA-interim and ECCO-v4 is roughly 5–10% of the mean precipitation over the Eastern Amundsen Sea, Prep150 and Prep50 are relatively large perturbations. An increase in precipitation enhances stratification and reduces vertical mixing between WW and CDW (Figure 12). Surface WW becomes saltier (fresher) and thicker (thinner) in the Prep50 (Prep150) simulation. The depths of the 34.2 and 34.5 isohalines do not change for the Prep150 simulation compared to the optimized simulation, while the depth of 34.2 contour is located at a depth of less than 50 m in the Prep50 simulation (Figures 12a and 12c). These changes are similar to the response to the increased surface sensible and latent heat fluxes (SF120 simulation, Figures 3a and 3b).

### 5. Summary

Recent observations as well as idealized modeling studies reveal that the thermocline depth or thickness of WW is important for controlling the PIG melt rate [Dutrieux *et al.*, 2014]. Despite the possible importance of WW thickness on ice shelf melting, previous modeling studies in this region have focused primarily on CDW

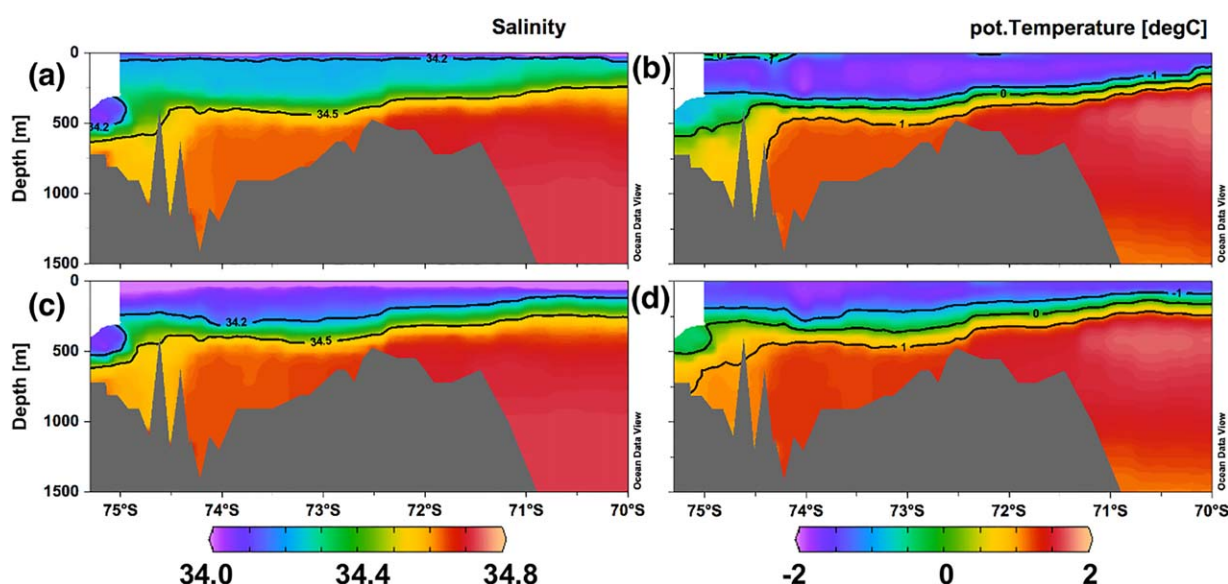


**Figure 12.** Simulated vertical sections of monthly mean (left) salinity and (right) potential temperature in January 2010 along the thick black line in Figure 1 for the (top) Prep50 and (bottom) Prep150 sensitivity simulations. For salinity, contours of 34.2 and 34.5 are shown with black lines. For potential temperature, contours of  $-1$ ,  $0$ , and  $1^{\circ}\text{C}$  are shown with black lines.

intrusion and have evaluated their simulations based only on bottom or deep CDW properties [e.g., *Thoma et al.*, 2008; *Holland et al.*, 2010; *Schodlok et al.*, 2012; *Assmann et al.*, 2013; *Nakayama et al.*, 2014a, 2014b; *St-Laurent et al.*, 2015; *Rodriguez et al.*, 2016]. As a result, none of these models have shown a good representation of WW in the AS. Since density of sea water is largely controlled by salinity at low temperature, the correct representation of WW properties, and thickness matters. In this study, we adjusted a regional Amundsen and Bellingshausen Seas configuration of the MITgcm, using forward sensitivity experiments and a Green's functions approach.

As a result of adjustments, our model shows significantly better match with observations than previous modeling studies, especially for WW (Figure 2). Based on the vertical section from trough E to PIG and horizontal sections at the 222 m and 552 m depths, we are able to represent spatial distributions as well as properties of WW and CDW that are close to observations (Figures 4 and 5). The depth of the thermocline and the 34.2 and 34.5 isohalines are also well reproduced. Since simulated hydrography of the AS shows a good agreement with observations, we also show the pathway of CDW intrusion and spreading of glacial meltwater (Figures 9 and 10) using passive tracers. Pathways of CDW intrusion and spreading of glacial meltwater are consistent with observations and modeling studies.

This is the first optimization study aiming to reduce the model-data difference (including ship-based and seal CTDs and satellite-based estimate of sea ice concentration and ice shelf melt rate) for the Amundsen and Bellingshausen Seas domain. To achieve better representation of WW and CDW, many forward sensitivity tests with different sets of model parameters are conducted. Then, a Green's functions approach [*Menne-menlis et al.*, 2005] is employed to further optimize the simulation by adjusting model parameters to minimize model-data difference in a least squares sense. Overall, the cost, which is defined as weighted model-data difference squared, is reduced by 23%. Note that we adjust turbulent heat and salt exchange coefficients for individual ice shelves. The different values of exchange coefficients are needed in order to have realistic amounts of freshwater and heat fluxes originating from the ice shelves, compensating for the coarse resolution of the simulation and the large representation errors.

We conduct sensitivity studies to investigate the impact of sensible and latent heat fluxes, PIG melt rate, and precipitation on the properties and thickness of WW in the eastern part of the AS. Model simulations are sensitive to sensible and latent heat fluxes and precipitation. WW properties become colder (warmer) and saltier (fresher) and the thermocline depth becomes deeper (shallower) with stronger (weaker) surface heat loss or less (more) precipitation (Figures 3 and 12). Although a previous modeling study points out that the local surface heat loss upstream of the Pine Island Polynya could be the reason for PIG melt decline

in 2012 [St-Laurent *et al.*, 2015], our model shows thickening of WW, a PIG melt decrease, and a WW salinity increase in response to the increased heat loss at the surface, rather than the observed WW freshening (i.e., deepening of 34.2 and 34.5 isohalines between 2010 and 2012). This suggests that changes in local surface heat loss or precipitation may not fully explain the 2012 Pine Island Glacier melt decrease. Sensitivity experiments also imply that freshening and cooling near PIG may be caused by an increase in basal melt rates of other glaciers upstream of PIG. Even though domain-wide constant changes of latent and sensible heat transfer coefficients are not the best representation of spatially and temporally localized processes in small coastal polynyas [St-Laurent *et al.*, 2015], our model sensitivity studies nevertheless emphasize that the freshening of WW observed in 2012 is an interesting conundrum deserving further investigation. Considering that cooling and freshening of WW is focused at middepth (250–600 m) but occurs in the large area (including the region ~120 km off the PIG front [Dutrieux *et al.*, 2014, Figure 2B], we speculate that observed cooling and freshening of WW in 2012 is likely related to both large scale ocean circulation change (forced by large scale wind forcing) as well as localized heat loss events as recently pointed out by Webber *et al.* [2017]. Further investigation requires model developments including adjustment of additional model variables or the refinement of model resolution.

Although this study provides a good representation of hydrography in the eastern AS for the period 2007–2010, further improvements are required including an improved representation of simulated sea ice, the extension of model simulations, as well as the refinement of model resolution. Model optimizations for these regions are important for (1) understanding oceanographic processes controlling the thermocline depth and PIG melt rate as well as (2) boundary forcing for ice sheet and regional ocean modelings. Moreover, the resolution of the regional domain (~10 km horizontal grid spacing) is comparable to that of current-generation IPCC (Intergovernmental Panel on Climate Change) global climate models and hence this study is expected to contribute to a better representation of these processes in IPCC-class global climate models. Our work is a first step toward an improved representation of ice-shelf ocean interaction in the ECCO (Estimating the Circulation and Climate of the Ocean) global ocean retrospective analysis.

# Acknowledgments

The research was carried out at the Jet Propulsion Laboratory, California Institute of Technology, under a contract with the National Aeronautics and Space Administration (NASA) and at the University of California, Irvine. Support was provided by an appointment to the NASA Postdoctoral Program; the NASA Cryosphere program; and the NASA Modeling, Analysis, and Prediction program. Computations were carried out at the NASA Advanced Supercomputing facilities. We thank Hong Zhang and Helene Seroussi for their useful comments and suggestions. Some of the figures are produced with Paraview and Ocean Data View [Schlitzer, 2004]. Model input and output data are available by contacting Y. Nakayama (Yoshihiro.Nakayama@jpl.nasa.gov). Insightful comments from two anonymous reviewers were very helpful for improving the manuscript.

# References

- Antonov, J. I., D. Seidov, T. P. Boyer, R. A. Locarnini, A. V. Mishonov, H. E. Garcia, O. K. Baranova, M. M. Zweng, and D. R. Johnson (2010), World Ocean Atlas 2009, in Volume 2: Salinity, NOAA Atlas NESDIS 69, edited by S. Levitus, Ed., 184 pp., U.S. Gov. Print. Off., Washington, D. C.
- Arndt, J. E., et al. (2013), The international bathymetric chart of the southern ocean (IBCSO) version 1.0 A new bathymetric compilation covering circum-Antarctic waters, *Geophys. Res. Lett.*, *40*, 3111–3117, doi:10.1002/grl.50413.
- Assmann, K., A. Jenkins, D. Shoosmith, D. Walker, S. Jacobs, and K. Nicholls (2013), Variability of circumpolar deep water transport onto the Amundsen Sea continental shelf through a shelf break trough, *J. Geophys. Res. Oceans*, *118*, 6603–6620, doi:10.1002/2013JC008871.
- Bamber, J. L., R. E. M. Riva, B. L. A. Vermeersen, and A. M. LeBrocq (2009), Reassessment of the potential sea-level rise from a collapse of the West Antarctic Ice Sheet, *Science*, *324*(5929), 901–903.
- Callahan, J. E. (1972), The structure and circulation of deep water in the Antarctic, in *Deep Sea Research and Oceanographic Abstracts*, vol. 19, pp. 563–575, Elsevier. [Available at <http://www.sciencedirect.com/science/article/pii/001174717290040X>.]
- Cavalieri, D., C. Parkinson, P. Gloersen, and H. Zwally (2006), Sea ice concentrations from Nimbus-7 SMMR and DMSP SSM/I passive microwave data, January 1979–June 2006, NSIDC DAAC: NASA DAAC at the National Snow and Ice Data Center, Boulder, Colo.
- Daru, V., and C. Tenaud (2004), High order one-step monotonicity-preserving schemes for unsteady compressible flow calculations, *J. Comput. Phys.*, *193*, 563–594.
- De Rydt, J., P. Holland, P. Dutrieux, and A. Jenkins (2014), Geometric and oceanographic controls on melting beneath Pine Island Glacier, *J. Geophys. Res. Oceans*, *119*, 2420–2438, doi:10.1002/2013JC009513.
- Dee, D., et al. (2011), The ERA-Interim reanalysis: Configuration and performance of the data assimilation system, *Q. J. R. Meteorol. Soc.*, *137*(656), 553–597.
- Depoorter, M., J. Bamber, J. Griggs, J. Lenaerts, S. Ligtnerberg, M. van den Broeke, and G. Moholdt (2013), Calving fluxes and basal melt rates of Antarctic ice shelves, *Nature*, *502*(7469), 89–92.
- Dinniman, M. S., J. M. Klinck, and W. O. Smith Jr. (2011), A model study of Circumpolar Deep Water on the West Antarctic Peninsula and Ross Sea continental shelves, *Deep Sea Res., Part II*, *58*(13), 1508–1523.
- Dinniman, M. S., J. M. Klinck, and E. E. Hofmann (2012), Sensitivity of Circumpolar Deep Water transport and ice shelf basal melt along the west Antarctic Peninsula to changes in the winds, *J. Clim.*, *25*(14), 4799–4816.
- Dutrieux, P., J. De Rydt, A. Jenkins, P. R. Holland, H. K. Ha, S. H. Lee, E. J. Steig, Q. Ding, E. P. Abrahamsen, and M. Schröder (2014), Strong sensitivity of Pine island ice-shelf melting to climatic variability, *Science*, *343*(6167), 174–178.
- Forget, G., J.-M. Campin, P. Heimbach, C. Hill, R. Ponte, and C. Wunsch (2015), Ecco version 4: An integrated framework for non-linear inverse modeling and global ocean state estimation, *Geosci. Model Dev.*, *8*(10), 3071–3104.
- Fox-Kemper, B., and D. Menemenlis (2008), Can large eddy simulation techniques improve mesoscale rich ocean models?, in *Ocean Modeling in an Eddying Regime*, edited by M. Hecht and H. Hasumi, pp. 319–338, AGU, Washington, D. C.
- Fretwell, P., et al. (2013), Bedmap2: Improved ice bed, surface and thickness datasets for Antarctica, *Cryosphere*, *7*(1), 375–393, doi:10.5194/tc-7-375-2013.
- Gaspar, P., Y. Grégoris, and J.-M. Lefevre (1990), A simple eddy kinetic energy model for simulations of the oceanic vertical mixing: Tests at station Papa and Long-Term Upper Ocean Study site, *J. Geophys. Res.*, *95*(C9), 16,179–16,193.
- Gent, P. R., and J. C. McWilliams (1990), Isopycnal mixing in ocean circulation models, *J. Phys. Oceanogr.*, *20*, 150–155.



- Hellmer, H., and D. Olbers (1989), A two-dimensional model for the thermohaline circulation under an ice shelf, *Antarct. Sci.*, 1(04), 325–336.
- Holland, P. R., A. Jenkins, and D. M. Holland (2010), Ice and ocean processes in the Bellingshausen Sea, Antarctica, *J. Geophys. Res.*, 115, C05020, doi:10.1029/2008JC005219.
- Hosking, J. S., A. Orr, T. J. Bracegirdle, and J. Turner (2016), Future circulation changes off west Antarctica: Sensitivity of the Amundsen sea low to projected anthropogenic forcing, *Geophys. Res. Lett.*, 43, 367–376, doi:10.1002/2015GL067143.
- Jacobs, S., C. Giulivi, P. Dutrieux, E. Rignot, F. Nitsche, and J. Mouginit (2013), Getz Ice Shelf melting response to changes in ocean forcing, *J. Geophys. Res. Oceans*, 118, 4152–4168, doi:10.1002/jgrc.20298.
- Jacobs, S. S., H. H. Hellmer, and A. Jenkins (1996), Antarctic ice sheet melting in the Southeast Pacific, *Geophys. Res. Lett.*, 23(9), 957–960.
- Jacobs, S. S., C. F. Giulivi, and P. A. Mele (2002), Freshening of the Ross Sea during the late 20th century, *Science*, 297(5580), 386–389.
- Jacobs, S. S., A. Jenkins, C. F. Giulivi, and P. Dutrieux (2011), Stronger ocean circulation and increased melting under Pine Island Glacier ice shelf, *Nat. Geosci.*, 4(8), 519–523.
- Jenkins, A., and S. Jacobs (2008), Circulation and melting beneath George VI ice shelf, Antarctica, *J. Geophys. Res.*, 113, C04013, doi:10.1029/2007JC004449.
- Jenkins, A., H. H. Hellmer, and D. M. Holland (2001), The role of meltwater advection in the formulation of conservative boundary conditions at an ice-ocean interface, *J. Phys. Oceanogr.*, 31(1), 285–296.
- Jenkins, A., K. W. Nicholls, and H. F. Corr (2010), Observation and parameterization of ablation at the base of Ronne Ice Shelf, Antarctica, *J. Phys. Oceanogr.*, 40(10), 2298–2312.
- Jourdain, N. C., P. Mathiot, N. Merino, G. Durand, J. Le Sommer, P. Spence, P. Dutrieux, and G. Madec (2017), Ocean circulation and sea-ice thinning induced by melting ice shelves in the Amundsen sea, *J. Geophys. Res. Oceans*, 122, 2550–2573, doi:10.1002/2016JC012509.
- Kim, I., D. Hahm, T. S. Rhee, T. W. Kim, C.-S. Kim, and S. Lee (2016), The distribution of glacial meltwater in the Amundsen sea, Antarctica, revealed by dissolved helium and neon, *J. Geophys. Res. Oceans*, 121, 1654–1666, doi:10.1002/2015JC011211.
- Large, W. G., and S. Pond (1982), Sensible and latent heat flux measurements over the ocean, *J. Phys. Oceanogr.*, 12(5), 464–482.
- Large, W. G., and S. G. Yeager (2004), *Diurnal to Decadal Global Forcing for Ocean and Sea-Ice Models: The Data Sets and Flux Climatologies*, Natl. Cent. for Atmos. Res., Boulder, Colo.
- Large, W. G., J. C. McWilliams, and S. C. Doney (1994), Oceanic vertical mixing: A review and a model with a nonlocal boundary layer parameterization, *Rev. Geophys.*, 32(4), 363–403.
- Li, X., D. M. Holland, E. P. Gerber, and C. Yoo (2014), Impacts of the north and tropical Atlantic ocean on the Antarctic peninsula and sea ice, *Nature*, 505(7484), 538–542.
- Locarnini, R. A., A. V. Mishonov, J. I. Antonov, T. P. Boyer, and H. E. Garcia (2010), World Ocean Atlas 2009, in *Volume 1: Temperature*, NOAA Atlas NESDIS 68, edited by S. Levitus, 184 pp., U.S. Gov. Print. Off., Washington, D. C.
- Losch, M. (2008), Modeling ice shelf cavities in a z coordinate ocean general circulation model, *J. Geophys. Res.*, 113, C08043, doi:10.1029/2007JC004368.
- Losch, M., D. Menemenlis, P. Heimbach, J.-M. Campin, and C. Hill (2010), On the formulation of sea-ice models: Part 1: Effects of different solver implementations and parameterizations, *Ocean Modell.*, 33, 129–144.
- Menemenlis, D., I. Fukumori, and T. Lee (2005), Using green's functions to calibrate an ocean general circulation model, *Mon. Weather Rev.*, 133(5), 1224–1240.
- Millan, R., E. Rignot, V. Bernier, M. Morlighem, and P. Dutrieux (2017), Bathymetry of the Amundsen Sea embayment sector of West Antarctica from operation ice bridge gravity and other data, *Geophys. Res. Lett.*, 44, 1360–1368, doi:10.1002/2016GL072071.
- Nakayama, Y., M. Schröder, and H. H. Hellmer (2013), From circumpolar deep water to the glacial meltwater plume on the eastern Amundsen Shelf, *Deep Sea Res., Part I*, 77, 50–62.
- Nakayama, Y., R. Timmermann, C. B. Rodehacke, M. Schröder, and H. H. Hellmer (2014a), Modeling the spreading of glacial meltwater from the Amundsen and Bellingshausen Seas, *Geophys. Res. Lett.*, 41, 7942–7949, doi:10.1002/2014GL061600.
- Nakayama, Y., R. Timmermann, M. Schröder, and H. Hellmer (2014b), On the difficulty of modeling Circumpolar Deep Water intrusions onto the Amundsen Sea continental shelf, *Ocean Modell.*, 84, 26–34.
- Nakayama, Y., K. I. Ohshima, Y. Matsumura, Y. Fukamachi, and H. Hasumi (2014c), A numerical investigation of formation and variability of Antarctic bottom water off Cape Darnley, East Antarctica, *J. Phys. Oceanogr.*, 44(11), 2921–2937.
- Nguyen, A., D. Menemenlis, and R. Kwok (2009), Improved modeling of the Arctic halocline with a subgrid-scale brine rejection parameterization, *J. Geophys. Res.*, 114, C11014, doi:10.1029/2008JC005121.
- Paolo, F. S., H. A. Fricker, and L. Padman (2015), Volume loss from Antarctic ice shelves is accelerating, *Science*, 348(6232), 327–331.
- Pritchard, H. D., S. R. M. Ligtenberg, H. A. Fricker, D. G. Vaughan, M. R. Van den Broeke, and L. Padman (2012), Antarctic ice-sheet loss driven by basal melting of ice shelves, *Nature*, 484(7395), 502–505.
- Randall-Goodwin, E. et al. (2015), Freshwater distributions and water mass structure in the Amundsen sea polynya region, Antarctica, *Elementa*, 3(1), 000,065.
- Redi, M. H. (1982), Oceanic isopycnal mixing by coordinate rotation, *J. Phys. Oceanogr.*, 12, 1154–1158.
- Rignot, E., S. S. Jacobs, J. Mouginit, and B. Scheuchl (2013), Ice-shelf melting around Antarctica, *Sci. Express*, 341, 226–270.
- Rintoul, S. R. (2007), Rapid freshening of Antarctic Bottom Water formed in the Indian and Pacific oceans, *Geophys. Res. Lett.*, 34, L06606, doi:10.1029/2006GL028550.
- Rodriguez, A. R., M. R. Mazloff, and S. T. Gille (2016), An oceanic heat transport pathway to the Amundsen Sea Embayment, *J. Geophys. Res. Oceans*, 121, 3337–3349, doi:10.1002/2015JC011402.
- Schlitzer, R. (2004), *Ocean Data View*, Alfred Wegener Inst. for Polar and Mar. Res., Bremerhaven, Germany.
- Schodlok, M. P., D. Menemenlis, E. Rignot, and M. Studinger (2012), Sensitivity of the ice shelf ocean system to the sub-ice shelf cavity shape measured by NASA Ice Bridge in Pine Island Glacier, West Antarctica, *Ann. Glaciol.*, 53, 156–162.
- Schodlok, M. P., D. Menemenlis, and E. Rignot (2016), Ice shelf basal melt rates around Antarctica from simulations and observations, *J. Geophys. Res. Oceans*, 121, 1085–1109, doi:10.1002/2015JC011117.
- Shepherd, A., et al. (2012), A reconciled estimate of ice-sheet mass balance, *Science*, 338(6111), 1183–1189.
- Sievers, H. A., and W. D. Nowlin (1984), The stratification and water masses at Drake Passage, *J. Geophys. Res.*, 89(C6), 10,489–10,514.
- Smith, D. A., E. E. Hofmann, J. M. Klinck, and C. M. Lascara (1999), Hydrography and circulation of the west Antarctic Peninsula continental shelf, *Deep Sea Res., Part I*, 46(6), 925–949.
- St-Laurent, P., J. M. Klinck, and M. S. Dinniman (2013), On the role of coastal troughs in the circulation of warm circumpolar deep water on Antarctic shelves, *J. Phys. Oceanogr.*, 43(1), 51–64.
- St-Laurent, P., J. Klinck, and M. Dinniman (2015), Impact of local winter cooling on the melt of Pine Island Glacier, Antarctica, *J. Geophys. Res. Oceans*, 120, 6718–6732, doi:10.1002/2015JC010709.

- Steig, E. J., Q. Ding, D. Battisti, and A. Jenkins (2012), Tropical forcing of circumpolar deep water inflow and outlet glacier thinning in the Amundsen sea embayment, west Antarctica, *Ann. Glaciol.*, **53**(60), 19–28.
- Stewart, A. L., and A. F. Thompson (2015), Eddy-mediated transport of warm Circumpolar Deep Water across the Antarctic Shelf Break, *Geophys. Res. Lett.*, **42**, 432–440, doi:10.1002/2014GL062281.
- Thoma, M., A. Jenkins, D. Holland, and S. Jacobs (2008), Modelling circumpolar deep water intrusions on the Amundsen Sea continental shelf, Antarctica, *Geophys. Res. Lett.*, **35**, L18602, doi:10.1029/2008GL034939.
- Turner, J., T. Phillips, J. S. Hosking, G. J. Marshall, and A. Orr (2013), The Amundsen sea low, *Int. J. Climatol.*, **33**(7), 1818–1829.
- Walker, D. P., M. A. Brandon, A. Jenkins, J. T. Allen, J. A. Dowdeswell, and J. Evans (2007), Oceanic heat transport onto the Amundsen Sea shelf through a submarine glacial trough, *Geophys. Res. Lett.*, **34**, L02602, doi:10.1029/2006GL028154.
- Walker, D. P., A. Jenkins, K. M. Assmann, D. R. Shoosmith, and M. A. Brandon (2013), Oceanographic observations at the shelf break of the Amundsen Sea, Antarctica, *J. Geophys. Res. Oceans*, **118**, 2906–2918, doi:10.1002/jgrc.20212.
- Webber, B. G., K. J. Heywood, D. P. Stevens, P. Dutrieux, E. P. Abrahamsen, A. Jenkins, S. S. Jacobs, H. K. Ha, S. H. Lee, and T. W. Kim (2017), Mechanisms driving variability in the ocean forcing of pine island glacier, *Nat. Commun.*, **8**, 14507.
- Wunsch, C., and P. Heimbach (2013), Dynamically and kinematically consistent global ocean circulation and ice state estimates, in *Ocean Circulation and Climate: A 21st Century Perspective*, chap. 21, edited by J. G. Gerold Siedler, S. M. Griffies and J. A. Church, pp. 553–579, Academic, New York.
- Zhang, X., A. F. Thompson, M. M. Flexas, F. Roquet, and H. Bornemann (2016), Circulation and meltwater distribution in the Bellingshausen Sea: From shelf break to coast, *Geophys. Res. Lett.*, **43**, 6402–6409, doi:10.1002/2016GL068998.